



# A self-contained, elastic joint drive for robotics applications based on a sensorized elastomer coupling—Design and identification

Jan Paskarbeits<sup>a,\*</sup>, Salvatore Annunziata<sup>a</sup>, Daniel Basa<sup>a</sup>, Axel Schneider<sup>b</sup>

<sup>a</sup> Research Group Biomechanics, Faculty of Technology, University of Bielefeld, P.O. Box 10 01 31, 33501 Bielefeld, Germany

<sup>b</sup> University of Applied Sciences, Faculty of Engineering and Mathematics, P.O. Box 10 11 13, 33511 Bielefeld, Germany

## ARTICLE INFO

### Article history:

Received 5 September 2012

Received in revised form 19 April 2013

Accepted 19 April 2013

Available online 15 May 2013

### Keywords:

Elastic joint drive

Compliant joint

Elasticity

Elastomer coupling

Compliance identification

System modeling

## ABSTRACT

While classical robotics traditionally makes use of stiff constructions in order to achieve a high precision, there is on-going research in development and control of new compliant robotic systems. These systems are suitable for direct human–machine–interaction due to their elastic behavior. The compliance is mostly achieved by control or by the integration of steel springs into the joint drives. This paper proposes a novel approach based on a sensorized elastomer coupling. Due to its damping characteristics, the interaction–safety can be improved in comparison to steel spring or purely control based approaches. The presented coupling is an integral part of a self-contained drive system which is also introduced. Simulation results of the strain/torsion and torque/torsion relationship for different geometrical variations of the elastomer coupling and experimental data of a prototype are presented. Since the sensorized coupling provides torsion measurements of the elastomer inlay, a system identification approach was employed to derive nonlinear and linear models of the coupling which can later be used in model-based joint-control.

© 2013 Elsevier B.V. All rights reserved.

## 1. Introduction

Classical drive systems for robotic joints are designed to be stiff in order to achieve high position accuracy and repeatability. If accuracy is of paramount importance, considerable attention has to be paid to mechanical construction, taking into account both torsional and bending stiffness in joints and segments. Stiff robots, however, are dangerous for humans when sharing the same workspace. A current topic in robotic research is the construction of compliant, light-weight joints with the objective to enhance safety especially in human–machine interaction. Additionally, compliance at the tool center point (TCP) could even be desired for the accomplishment of some tasks (for example peg-in-hole or bead-on-a-wire tasks [1]). Compliant behavior can be achieved, e.g. by hybrid control [2], impedance control [3] or passivity based impedance control [4]. In these systems compliance is mimicked by control. Other approaches to produce adjustable compliance make use of serial elastic elements, e.g. steel springs, between the actuator and the output of the drive [5–9]. When using steel springs, special attention has to be paid to the springback of the drive system due to the low damping characteristics. In addition, systems with steel springs require a large design envelope for the accommodation of the support structures for the springs. This also

increases the overall weight of the drive system (an overview of current compliant joint architectures can be found in [10]).

In this work, a new sensorized elastomer coupling based on the principle of jaw couplings is presented. The elastomer material serves both as a serial elastic element and as a damper. Using an absolute rotary position sensor, the torsion angle of the coupling can be measured. This information can then be used to estimate the torque acting on the coupling. Due to the optimization of space requirements, this coupling can easily be integrated into a drive train. In this work, the coupling is integrated into a self-contained, rotatory joint drive designed for robotics applications. The design of the drive system with the sensorized elastomer coupling is presented in Section 2. In order to optimize the elasticity characteristic of the elastomer coupling different jaw geometries were evaluated in simulation as well as experimentally. These results are presented in Section 3. As the elastomer coupling has a high damping factor as compared to steel spring based designs, this must be considered for the torque estimation. Therefore, the second part of this work, starting with Section 4, is dedicated to the system identification and modeling of the elastomer coupling based on test data. Starting from black-box nonlinear identification methods, a two-step procedure is used to optimize the model. Due to the limited computational capacity of the drive's embedded microcontroller, a linear model of the elastomer coupling would be desirable to reduce the complexity of the required calculations for control approaches.

With the objective to find a reduced order linear dynamic model of the elastomer coupling simple stretch–strain lumped models are

\* Corresponding author. Tel.: +49 521 106 5191; fax: +49 521 106 6440.

E-mail address: [jan.paskarbeits@uni-bielefeld.de](mailto:jan.paskarbeits@uni-bielefeld.de) (J. Paskarbeits).

**Table 1**  
Technical data of the rotatory drive.

Parameter	Value	Unit
Length	~90	mm
Diameter	~52	mm
Max torque	~15	Nm
Weight	~0.390	kg
Power/weight	~170 <sup>a</sup>	W/kg

<sup>a</sup> Upgradable to 400 W/kg.

evaluated and tested in a gray-box identification approach in Section 5. The presented evaluation results confirm that such linear models produce performances comparable to the nonlinear models.

## 2. Self-contained, elastic joint drive

The rotatory drives were designed for the application in robotic limbs, for example in the legs of walking robots [11,12]. Therefore, one basic requirement was that the drives must be able to generate sufficient torques able to support the weight of the robot – in case they are used as leg actuators – or the weight of the subsequent segments – if they are used in a robotic arm. In both cases, the weight of the robot/subsequent arm segments is mainly governed by the weight of the integrated drives. As a consequence, a main aspect during the design of the drives was a high torque/mass-ratio.

The technical data of the drive is listed in Table 1. In order to reduce the cabling and to allow autonomous operation, the control and power electronics were integrated into the drive (see Fig. 1(b)). The power electronics, built up of three half-bridges and a gate driver, is able to deliver currents up to 69 A. As the motor is designed for a voltage of 24 V, whereas the driver electronic is able to operate at voltages up to 40 V, temporary overloads are possible as long as the maximum stator coil temperature is not exceeded. Since the stator currents and the motor temperatures are sensed continuously, a breakdown of the stator winding insulation can be prevented by in time power reduction. Using up-to-date power MOSFETs with an extremely low on-resistance, the power dissipation of the driver electronics could be vastly reduced. Therefore, it is possible to place it within the actuator housing without the danger of overheating although no active cooling measures have been integrated. Using a sinusoidal commutation schema, the torque ripple is reduced as compared to block commutation or mechanically commutated motors. The commutation is controlled by the embedded microcontroller that is also used for the acquisition of local sensor signals (positions, temperatures, phase currents) and the communication with external controllers via a differential bus system. This enables the decentral application of velocity/position control as well as bio-inspired control approaches. With the objective to build lightweight robot-drives, which provide safe interactions both with humans and with unknown environments, a serial elastic element was designed and integrated into the drive. The usual way to generate elastic interactions using “stiff” actuators is based on active stiffness control and can be realized for example with the integration of a torque sensor between the gearbox and the output of the drive. In this case, the use of sensors and control strategies based on feedback signals ensures the system to reach the desired dynamic behavior between the end effector and the external force acting on the link side [4,13,14]. The advantage of this approach is the ability to change the elasticity online while a drawback is the need for controllers that are fast enough to cope with high torque peaks acting on the output link of the drive. For example, during collisions of the limb with the environment, high torque peaks may occur in the joint drive which could be harmful both for the gearbox and the environment. These disadvantages can be eluded with

the integration of an inherently elastic element which reduces high torque peaks [15,16]. In the drive setup presented in this work an elastic element is placed between the gearbox and the output link. Furthermore, by measuring the torsion of the elastic element, the acting torques can be calculated if a model of the elastic element is provided. In this way, the elasticity of the drive can be varied and even be suppressed by control without the need for additional torque sensors. In contrast to the exclusively controlled elasticity, the inherent elasticity is also maintained in cases of outage, control errors, etc. [17,18,7,8].

### 2.1. Integrable, sensorized elastomer coupling

A new sensorized elastomer coupling based on the principle of jaw couplings is integrated into the drive (see Fig. 2). The coupling consists of three parts: Two metallic hubs with three axially protruding teeth (jaws) that gear into each other but still leave room for an elastic element in the center. This elastic element consists of a central ring with six radially protruding lobes. The lobes fit in between the metallic teeth of both hubs. A torque acting between the two hubs results therefore in a compression of the elastic lobes. This design can be easily integrated into a drive system as only minimal support structure is required. As opposed to steel springs with a low attenuation, elastomer-based couplings reduce the potentially harmful undamped resilience in the output due to their comparably high damping characteristics. Furthermore, by chemical/physical modification of the inlay, e.g. by adding adequate fillers, the damping attenuation of the elastomer can also be changed.

In order to be able to compute the acting torque based on the torsion of the elastic coupling, an angular encoder must be integrated into the drive. A Hall-effect based encoder IC that measures the angular position of a diametrically magnetized permanent magnet was chosen due to its small size and the high angular resolution of 12 bit. The encoder is connected to the output side of the coupling whereas the magnet is fastened to a pin protruding from the input flange. For the precise measurement of the output position (joint angle) an additional angular encoder is integrated whose sensor board is placed back-to-back to the first one. The permanent magnet associated to the joint angle measurement is connected to the housing of the drive (not shown in Fig. 2(b)). Since the magnetic field of the torsion-measurement-magnet also influences the position-measurement-sensor and vice versa, a magnetic shielding, consisting of high-permeability sheets, is placed between the sensor boards to reduce crosstalk.

In commercially available jaw couplings only half of the lobes account for the generation of a restoring torque whereas the other lobes are unloaded. The presented elastomer coupling, however, uses all lobes to generate elastic restoring forces. This result is achieved by bonding the faces of the lobes to the metallic faces of the jaws. In this way, during a relative twist between input and output flange, half of the lobes are stretched and the other half is compressed. A consequence of this technical solution, as it will be shown at the end of Section 3, is an increased maximum torque that the coupling is able to withstand.

## 3. Elastomer coupling design and torque–torsion optimization based on different jaw geometries

In order to center the inlay during load phases, commercially available couplings use concave jaw faces. An example is depicted in Fig. 3(a). For the bonded inlay, however, a concave shape is not important since the position of the inlay is determined by the connected faces of the inlay and the jaws. Nevertheless, the geometry of the jaws – and as a consequence the geometry of the inlay – influences the elasticity characteristics. With the objective to

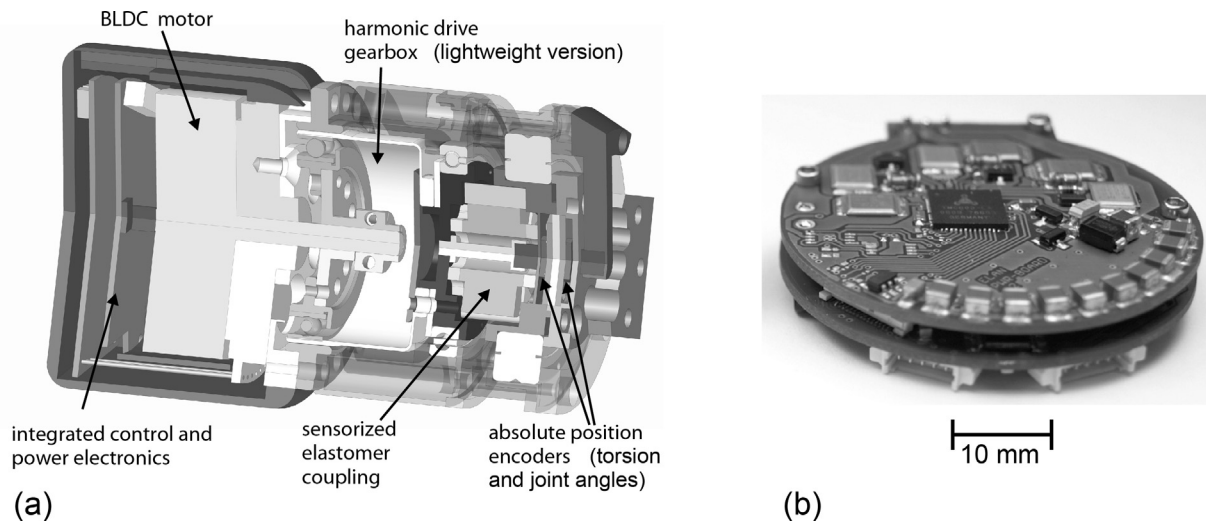


**Fig. 1.** (a) Section view of the elastic rotatory drive for actuation of robotic joints. The self-contained drive contains a power- and control-electronics stack (see (b)), a BLDC motor with external rotor, a lightweight Harmonic Drive gearbox, a novel, sensorized, elastomer coupling, two position encoders for the measurement of torsion and joint angles. (b) Image of the power- and control-electronics stack which is mounted in the back of the drive.

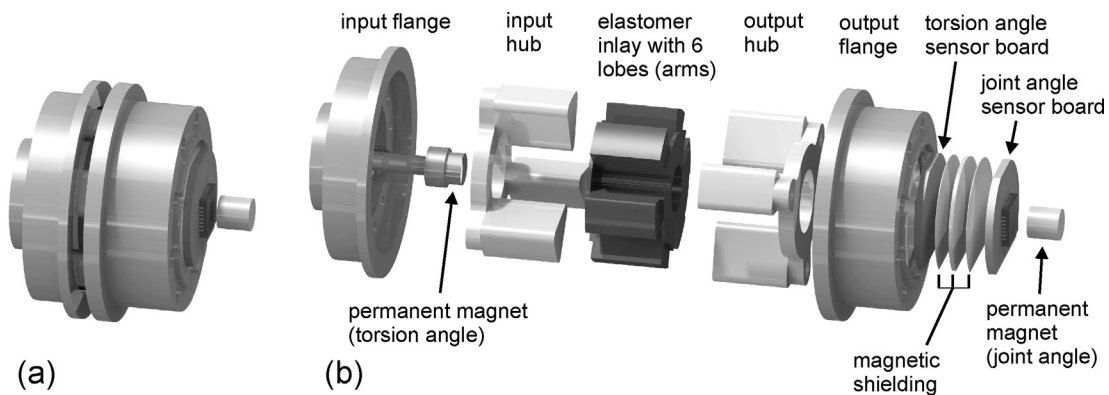


**Fig. 2.** (a) View of the new, sensorized elastomer coupling as integrated into the rotatory drive. (b) Explosion view of the sensorized elastomer coupling shown in (a). The input flange is mechanically connected to the output of the gearbox (flexspline), pivoted in a four point contact bearing (not shown). The output flange is mechanically connected to the output disk which is pivoted in a cross roller bearing (not shown). The input hub has three teeth or jaws and is fixed to the input flange. The output hub has also three teeth and is fixed to the output flange (form closure). The torque between input and output is transmitted via a six-armed elastomer inlay which is inserted in-between the hubs. The torsion (twist) between input hub and output hub is measured by means of a Hall-effect position sensor (torsion angle sensor). This sensor faces a diametrically magnetized permanent magnet which is attached to a pin jutting out from the input flange. When assembled, the magnet on the pin dives through the holes of the hubs and elastomer inlay and arrives in front of the torsion angle sensor. In order to measure the output position of the joint, a position sensor board is mounted back-to-back to the torsion angle sensor board and faces a second, diametrically magnetized permanent magnet. Three layers of magnetic shielding have been added between the back-to-back sensors to suppress the influence of the magnet on the other side.

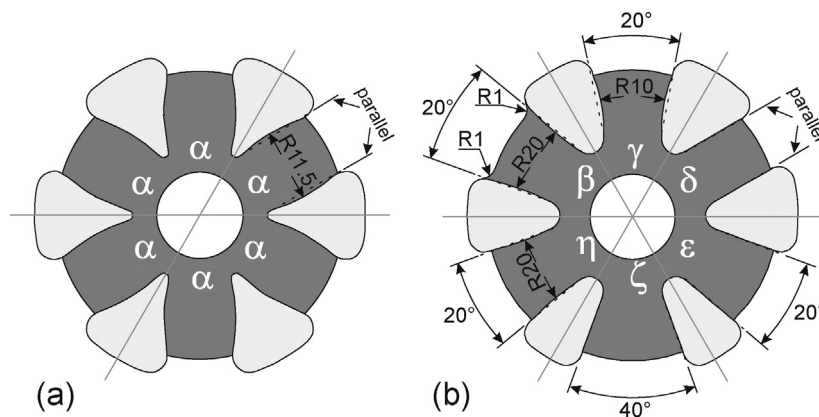


**Fig. 3.** Front view of the elastomer inlay with the metallic faces of the jaws: Evaluation of seven different jaw geometries. (a) The inlay for geometry  $\alpha$ : Side flanks of the jaws are parallel and have a concave shape (radius = 11.5 mm). (b) The other inlay geometries ( $\beta, \dots, \eta$ ). Geometry  $\beta$  presents side flanks of the jaws inclined by  $20^\circ$  and a convex shape (radius = 20 mm).  $\gamma$ : Same as  $\beta$  but the convex shape has radius = 10 mm.  $\delta$ : Side flanks of the jaws are parallel and straight (no convexity).  $\epsilon$ : Side flanks of the jaws are inclined by  $20^\circ$  and straight.  $\zeta$ : Side flanks are inclined by  $40^\circ$  and straight.  $\eta$ : Side flanks are inclined by  $20^\circ$  and convex (radius = 20 mm).

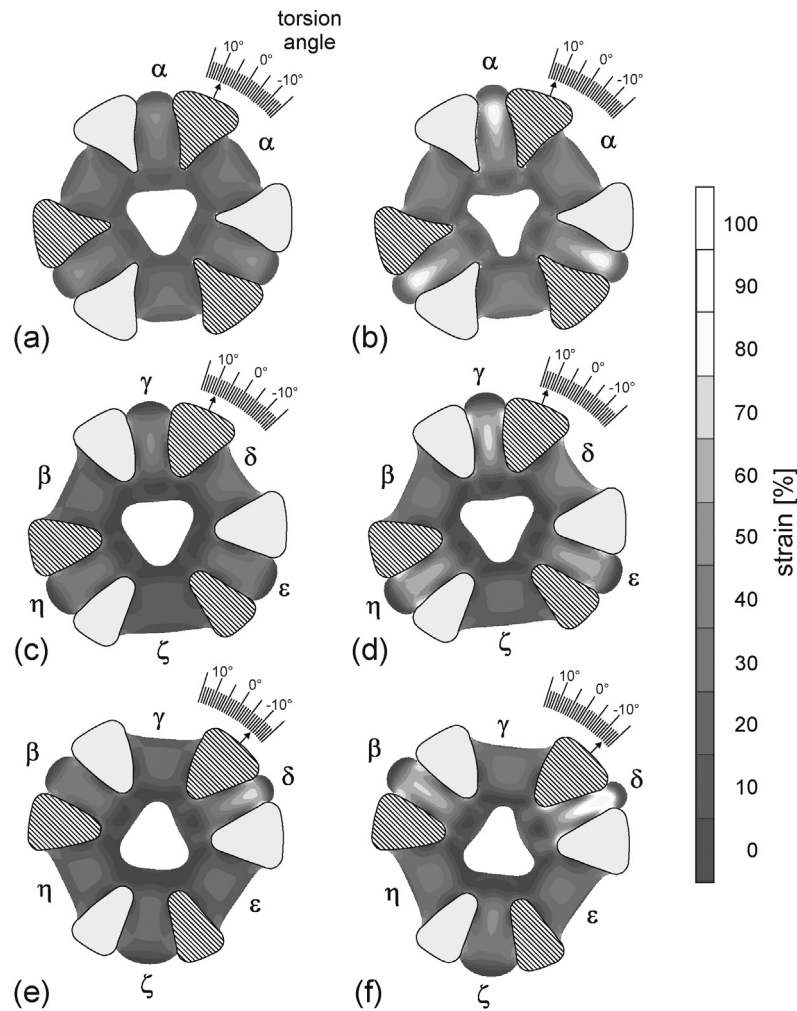


**Fig. 4.** Results of FEM simulation for seven different jaw geometries showing deformation and strain of the lobes in correspondence to two torsion angles. The left column (a, c, e) shows the elastomer deformation for a torsion of  $\pm 9^\circ$ , the right column (b, d, f) shows the deformation for a torsion of  $\pm 12^\circ$ . The upper row (a and b) depicts the results in the case of elastomer completely based on jaw geometry  $\alpha$ . (c–f) The simulation results in case of a single elastomer constructed with the other geometry profiles ( $\beta, \dots, \eta$ ). For the other geometry profiles ( $\beta, \dots, \eta$ ) the simulation results are shown in (c–f).

find out how the geometry of the elastic element influences the torque–torsion characteristic, several jaw geometries were tested in finite-element-method (FEM) simulations. The most important results that can be obtained from these simulations are the maximum strain of the elastic material and the torque that is produced for a given torsion angle. As polymers tend to fatigue if they are strained beyond certain limits, the angle dependent nominally permissible strain in the material confines the maximal torsion angle which in turn defines the maximal torque that can be produced by the coupling in nominal operation. This maximal torque can be increased by increasing the diameter and/or the length of the coupling. Therefore, an optimization of the stress–strain characteristics of the coupling, in particular an increase of the maximal acceptable torque can be used to reduce the needed length/diameter for a given maximal load. On the other hand, an increased permissible torsion angle results in an increased resolution for the torque estimation that is based on the torsion angle measurement. The stiffness characteristic of the elastic element is also influenced by the shore hardness of the elastic material. However, the material must be selected also under consideration of its tendency for plastic deformation. The presented results refer to a coupling with a length of 10 mm, a diameter of 20 mm and an elastomer (SPP1838/81; Kraiburg, Waldkraiburg, Germany) with shore hardness of 94 A.

This elastomer has a compression set of 4%<sup>1</sup> which indicates a low tendency to undergo permanent deformations when subject to compression. Although the compression set value is low, for this material it is suggested to limit the maximum strain to 60%.

As a first trial, the already mentioned convex geometry that is based on commercially available jaw couplings (see Fig. 3(a)) was tested in a two dimensional FEM simulation (MSC Software Corporation, Santa Ana, CA, USA). In the simulations, the strain of the elastic material and the torque transmitted for a given torsion angle were evaluated.

This geometry consists of six congeneric elastomer lobe geometries. Exemplary results of the FEM analysis are shown in Fig. 4(a) and (b). Since the strain in the vicinity of the central ring of the elastomer inlay and therefore the influence of the lobes onto each other is considered to be negligible, further elastomer lobe geometries were integrated into a single test coupling for simulation purposes (see Fig. 3(b)). These geometries also include straight and concave faces. Moreover, different face angles with respect to the middle axis were used for the straight faced jaws. In order to reduce the

<sup>1</sup> Value obtained for the elastic material subject to a compression of 15% after 24 h at a temperature of 23 °C.

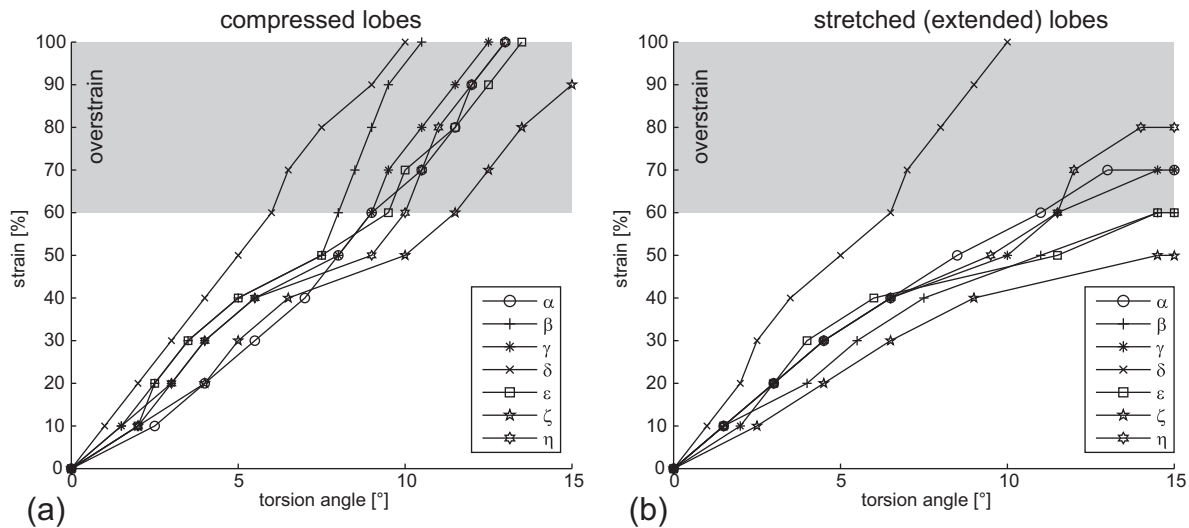


**Fig. 5.** Simulation results of strain plotted over torsion angle for different jaw geometries. (a) Reports the case of compressed lobes. (b) Same as (a) but for stretched (extended) lobes.

strain at the onset of the elastic element to the metallic jaws, a tapering radius was tentatively introduced for geometry  $\beta$ . The exemplary results of the analysis for these geometries are depicted in Fig. 4(c)–(f). For a given torsion angle, the strain in the elastomer material depends on the elastomer lobe geometry. For example, geometry  $\delta$  reaches a strain of 90% already at a compression of 9° (see Fig. 4(e)) whereas the strain for geometry  $\zeta$  stays below 60% even at a compression of 12°.

### 3.1. Elastomer simulations – torsion–strain characteristics

The strain of the elastic material was computed in the torsion interval from  $-15^\circ$  to  $15^\circ$  for all seven elastomer lobe geometries ( $\alpha, \dots, \eta$ ). The torsion–strain results of the simulations are depicted in Fig. 5(a) for compressed and in Fig. 5(b) for stretched lobes. It can be seen that geometry  $\zeta$  has the lowest strain both for compression and extension. The reason for that is that the angle between the faces and the middle axis of the jaws is minimal (as shown in Fig. 3(b)) compared to the other geometries, which results in a maximal width of the elastic lobe. The strain can therefore be distributed across a wider segment of material. The opposite applies for geometry  $\delta$  due to the comparably small width of the material at the outer face. The other geometries have a nearly comparable stress–strain behavior. Furthermore, except for geometry  $\beta$ , the strain of the extended lobes is smaller than the strain of the compressed lobes for equal torsion angles.

In order to further increase the maximally applicable torque, the geometry of the jaws should be optimized to equalize the strain for compression and extension of the lobes.

### 3.2. Elastomer simulations – torsion–torque characteristics

In contrast to the strain of the material, the pressure acting on the protruding faces of the hubs and accordingly the transmitted torque is strongly dependent on the material properties. Using the specified shore hardness a qualitative torsion–torque characteristic can be estimated (see Fig. 6). However, in order to gain reliable quantitative results from the simulation, the parameters adopted for the simulation should be tuned based on the application and experimental data. The torque related simulation results are therefore only comparable among each other.

As it could be expected, the jaw geometry with the highest strain for a given torsion angle, geometry  $\delta$ , produces the highest torque

at each torsion angle. Accordingly, geometry  $\zeta$  produces the lowest torque. However, in order to find the coupling that is able to withstand the highest torques, the torques that are produced for a strain of 60% (i.e. before overstrain is reached) by the different jaw geometries have to be compared.

These torques and the corresponding torsion angles are listed in Table 2. According to these results, jaw geometry  $\eta$  is able to withstand the highest torques, followed by geometry  $\alpha$ .

### 3.3. Results of torque–torsion tests

As mentioned before, the parameters adopted in simulation must be fine-tuned based on experimental data in order to give reliable quantitative results. In order to experimentally test the elastic element, a first prototype of the coupling was manufactured and integrated into the drive. For the selection of the jaw geometry, it was observed in the former section that  $\alpha$  and  $\eta$  show the best performances in terms of maximum torque. Since geometry  $\alpha$  has a self-centering effect on the elastomer inlay due to its concave shape, it was preferred over geometry  $\eta$ . In this way, both unbonded

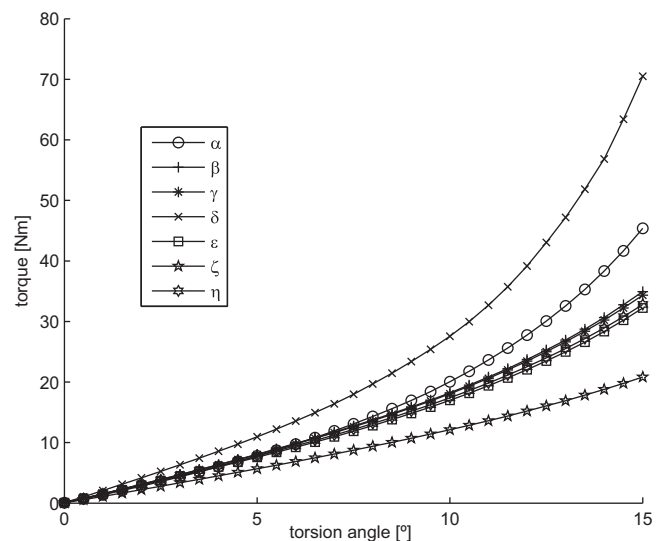


**Fig. 6.** Torque values plotted over torsion angle obtained in simulation for different jaw geometries ( $\alpha, \dots, \eta$ ).



**Table 2**  
Maximum permissible torsion angle and corresponding deliverable torque

Geometry	$\alpha$	$\beta$	$\gamma$	$\delta$	$\epsilon$	$\zeta$	$\eta$
Max. torsion angle for strain $\leq 60\%$ ( $^\circ$ )	9.0	8.0	9.0	6.0	9.5	11.5	10.0
Torque for max. torsion angle (Nm)	17.0	13.8	15.7	13.6	15.9	14.4	17.4

and bonded elastic inlays could be tested and comparisons between the two distinguished approaches could be made. To test the elastic behavior of the elastomer coupling, a lever arm was connected to the output shaft of the drive. Slow rotations of the lever arm with a mass attached at the extremity were performed for increasing load torques up to 6 Nm (torque upper limit). Once the upper limit was reached, the rotary movement was reversed until the negative maximum load of  $-6$  Nm was reached. This cycle was repeated 30 times.

The experiment was conducted both with a loose (unbonded) elastomer inlay inside the coupling and with a bonded version. Fig. 7 depicts the results of the experiment. In correspondence to the maximum load ( $\pm 6$  Nm) the unbonded coupling was subject to a torsion of  $\pm 11.5^\circ$ , while for the bonded coupling the torsion was of only  $\pm 8^\circ$ . Since the first cycles are depicted in light gray and later cycles are displayed in darker shades of gray, the path/time-dependency can be traced. For this test, the elastomer lobes have simply been glued to the metal faces using Loctite 770 & 406 (Henkel, Düsseldorf, Germany). The advantage of this bonding technique is the simple assembly. The disadvantage is the low stability of the connection. As this test was a mere step to find out in which way the unbonded and the bonded versions differ under load, the long-term stability was not important. Therefore, the hysteresis curve of the bonded version changes over time since the connected area between metal and elastomer parts decreases. Over a longer period, it would likely resemble the curve of the unbonded version. However, in the beginning, the bonded version is 1.4 times stiffer than the unbonded version. This result confirms that by bonding the elastomer inlay to the adjacent metallic faces of the coupling a stiffer elastomer coupling can be built. The hysteresis effect observable in both curves is a general property of elastomers and can be attributed to the high damping characteristics of such materials. However, the magnitude of this hysteresis depends on the

cross-link of the material and on the bulking agents used to modify the material characteristics. The load- and the unload-curves of the unbonded elastomer inlay meet at the origin of the coordinate system. The curves of the bonded coupling keep a certain distance from each other. The reason is that in the unbonded coupling, only three lobes of the elastomer inlay are deformed during the load-phase whereas the other three lobes remain unloaded. During the unloaded phase, the lobes can regain their original shape and after a load reversal each load curve is started with originally shaped elastomer lobes. In the connected coupling, however, all six lobes are deformed during each load phase. Therefore, the elastic curve for a new load phase depends on the previous history of the coupling.

#### 4. Nonlinear modeling of the elastomer coupling using measured data

An exact mathematical representation of the elastomer coupling cannot be obtained a priori from physical considerations due to its nonlinear behavior. Therefore, a two-steps identification algorithm has been adopted for modeling. First, a black-box modeling identification was carried out – in this way the structure of the system that performs best is obtained [19]. Then, a second identification step based on the prediction-error method was applied to the system in order to further improve the model estimation [20, Chapter 2].

##### 4.1. Experimental setup and data measurement

To develop a model of the black-box system a data-driven modeling approach is pursued. Data-driven modeling is based on generating input signals and measuring the resulting output. The measurements are then used to derive the dynamic model. Input signals have to be constructed in order to excite the modes of the system to identify and capture its dynamics. With the objective to record the data for the identification of the elastomer coupling, the output shaft of the drive was connected to a torque sensor (ME-Messsysteme GmbH, Hennigsdorf, Germany) and then clamped. A rotation of the motor therefore results in a torsion of the elastomer coupling (a deformation of the elastomer lobes) and a change of the torque measured by the torque sensor. A feedback control loop with a PI controller was used to control the torque. The *estimation data* (data set used to fit the model) and the *validation data* (data set used for model validation purposes) were collected for several triangularly shaped torque input amplitudes and frequencies. The measurements were conducted with a sampling rate of 200 Hz. The desired input torque varied within the range of  $[-5, \dots, 5]$  Nm and a frequency of  $[0.4, \dots, 4]$  Hz. The angular deflection corresponds to the input of the black-box representing the model of the elastomer coupling while the torsion measured by the torque sensor corresponds to its output. As mentioned in Section 3, the glued connection between the elastomer and the metal parts is not very durable. In order to increase the durability of the coupling, the elastomer was bonded to the primer-coated metal parts directly during the vulcanization process. However, since this was the first experiment using vulcanization-bonded couplings, geometry  $\epsilon$  was chosen due to its reduced strain/torsion-ratio for the stretched elastomer lobes compared to geometry  $\alpha$  (see Fig. 5(b)). Therefore, the strain in the stretched lobes is reduced. As the vulcanization-bonding-process involves many variables such as the

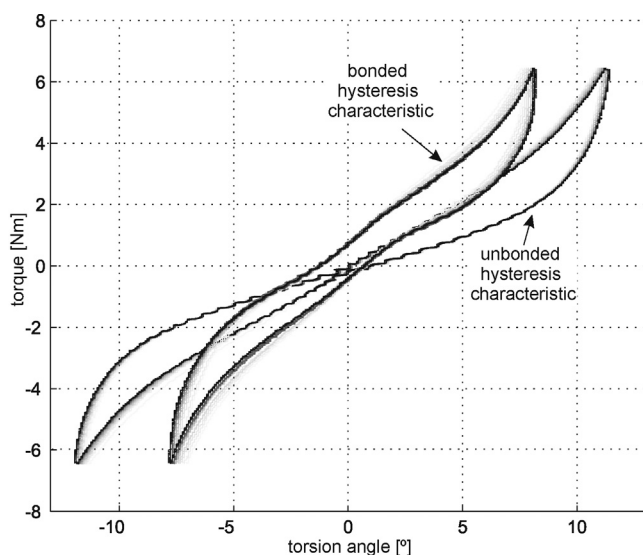


**Fig. 7.** Experimental elastic characteristics of jaw geometry  $\alpha$ . The measured load torque is plotted over the torsion angle for both bonded and unbonded elastic inlays. Data were collected for thirty cycles of torque load spanning in the range ( $-6, \dots, 6$  Nm). The first cycles are displayed in light gray, the later cycles are displayed in darker shades.

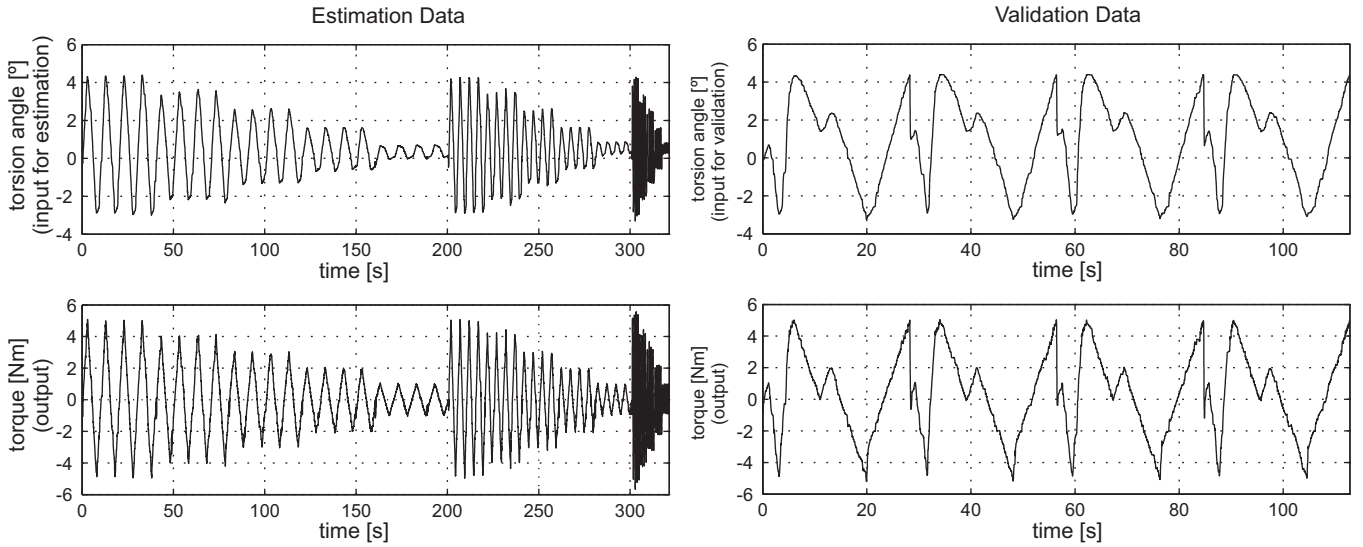


**Fig. 8.** Estimation and validation data. Left column shows input (upper panel) and output data (lower panel) used for the system identification process. Right column shows input (upper panel) and output data (lower panel) used for the validation of the models.

elastomer–primer matching, the temperature profile during the vulcanization and the addition of potentially bond-strengthening additives, the bonding optimization has not yet been finished. For the first prototypes, a long-term stable bond between the metal and the elastomer up to torques of 8–10 Nm has been achieved. However, in order to avoid any kind of flaking of the elastomer from the metal teeth faces, the maximum torque for the model design was reduced to  $\pm 6$  Nm. As the zero crossing, which is the most critical point because of the hysteresis effect, has been included both in the estimation and validation data, the extension of the maximum torque range of the model for an enhanced elastomer coupling is not expected to be a problem. The measured data sets are shown in Fig. 8.

#### 4.2. Black-box modeling

The black-box modeling approach is a trial and error process based on the evaluation of identification results coming from various model structures and their comparison.

##### 4.2.1. Model structure evaluation

With the objective to produce the black-box continuous time (CT) model of the elastomer coupling from its sampled input–output data, the indirect approach is followed [21, Chapter 2]. In this case, by applying discrete time model estimation methods to the sampled data, the discrete time (DT) model is obtained first. In a second step, the DT model is transformed into CT form. In this approach, different model structures available in the Matlab® System Identification Toolbox™ (The MathWorks Inc., Natick, MA, USA) were tested and their results were compared.

A test to quantize the ability of the model to describe the data is given by the calculation of the best fit (BF). The BF indicates the percentage of agreement between the predicted model output  $\hat{\mathbf{y}}$  and the measured output  $\mathbf{y}$  (100% means a perfect fit)

$$\text{BF} = \left( 1 - \frac{\|\mathbf{y} - \hat{\mathbf{y}}\|}{\|\mathbf{y} - \bar{\mathbf{y}}\|} \right) \cdot 100\% \quad (1)$$

with  $\bar{\mathbf{y}}$  being the mean of  $\mathbf{y}$ . In the following, BF calculation is always performed based on the validation data.

As it has been observed in Section 3, the system that has to be identified contains nonlinearities (see Fig. 7). Therefore, this work aims for a nonlinear model structure in the identification

process. While modeling lumped linear systems is relatively straightforward, strategies for modeling nonlinear systems are less evident due to the huge amount of possible nonlinear structures (nonlinear state-space models, NARMAX models [22], neural networks, etc.). One class of nonlinear identification structures is the NonLinear-AutoRegressive-with eXogenous-inputs (NLARX) approach. Another class is the Hammerstein–Wiener-model (HW-model). While HW-models can only model static nonlinearities, NLARX models can model also dynamic nonlinearities.

For simplicity, the HW-model has been chosen as model structure for the identification in this work. Such a model is composed by a static input–nonlinearity (uNL), a linear dynamic system ( $G_d$ ) and a static output–nonlinearity (yNL). The complete HW-model structure, indicating input and output variables for each block is shown in Fig. 9.

As input- and output-nonlinearities, polynomial and piecewise linear approximation functions were evaluated as those seem to be the most adequate to describe the behavior shown in Fig. 7.

In the trial and error simulations according to the black-box modeling approach, several polynomial and piecewise linear approximation functions were evaluated for the different parts of the HW-model. The final version of the model in this work reaches a BF of 77.73%. In this version, the input nonlinearity (uNL) and the output nonlinearity (yNL) can be represented by a second and a third order polynomial, respectively. These polynomials have the form:

$$w = 3.4 \cdot 10^{-2} u^2 + 1137.56 u - 226.65 \quad (2)$$

$$y = -0.141 \cdot 10^{-10} x^3 - 0.649 \cdot 10^{-7} x^2 + 0.187 \cdot 10^{-2} x + 0.309 \cdot 10^{-1} \quad (3)$$

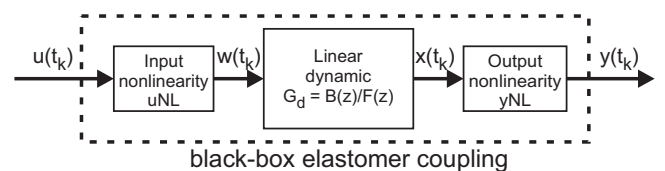


**Fig. 9.** Hammerstein–Wiener model with input and output signals indicated for each block.

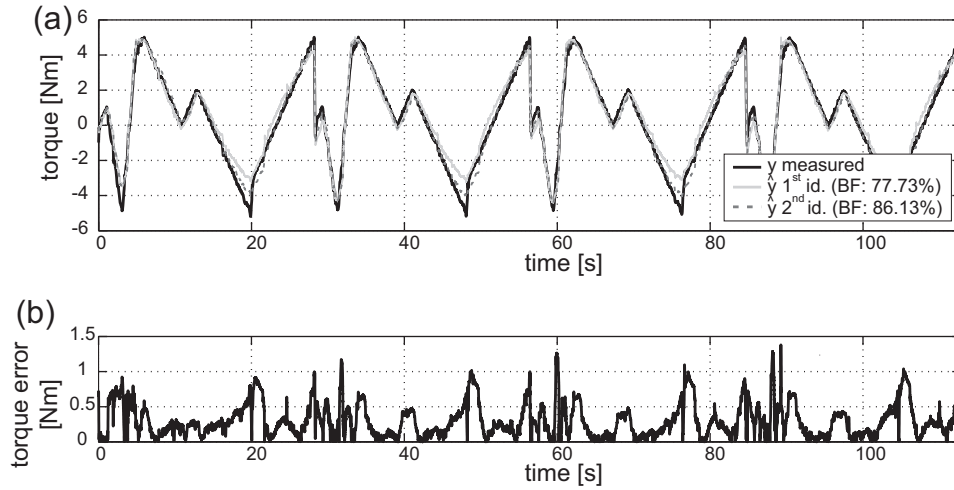


**Fig. 10.** (a) Best fit evaluation after the 1st and 2nd identification step. (b) Torque error of the model after the 2nd identification step.

The identification approach delivers the linear dynamic system  $B(z)/F(z)$  between input  $w(t_k)$  and output  $x(t_k)$  in discrete-time form:

$$x(t_k) = \frac{B(z)}{F(z)} w(t_k) + e(t_k) \quad (4)$$

with the model disturbance  $e(t_k)$  and

$$B(z) = 1 - 0.9989z^{-1} \quad (5)$$

$$F(z) = 1 - 0.5793z^{-1} - 0.417z^{-2} \quad (6)$$

where  $z^{-1}$  is the backward shift operator. This linear dynamic system can be expressed as discrete transfer function:

$$G_d(z) = \frac{z \cdot (z - 0.9989)}{(z - 0.9973) \cdot (z + 0.4181)} \quad (7)$$

The parameters of the DT model are functions of the sampling rate and normally do not have direct physical meaning [21, Chapter 1], [23]. Therefore, the idea is to transform  $G_d$  into a CT model  $G_c$  which represents the underlying physical system.

By using the transformation method according to *Tustin*, the CT transfer function  $G_c$  in the Laplace variable  $s$  is obtained:

$$G_c(s) = \frac{1.72 \cdot s^2 + 688.3 \cdot s + 152.2}{s^2 + 975.3 \cdot s + 520.1} \quad (8)$$

In the following, the CT model is further optimized in the continuous time domain.

#### 4.3. Black-box modeling – second step

In order to further improve the BF of the model, the parametrized CT transfer function of the linear dynamic (8) obtained in the model structure evaluation, is further optimized using a *prediction-error method* [20, Chapter 7] while the linear input and output transfer functions ((2) and (3)) remain the same.

The parametric model of the linear dynamics (in the Laplace domain) between the input  $X(s)$  and the output  $W(s)$  has the following general structure:

$$\frac{W(s)}{X(s)} = \frac{a_1 s^2 + b_1 s + c_1}{a_2 s^2 + b_2 s + c_2} \quad (9)$$

With the vector of unknown parameters  $\lambda = (a_1, \dots, c_2)$  and the time instants  $t_k = kT_s$ , the prediction error of the complete model is:

$$\epsilon(t_k, \lambda) = y(t_k) - \hat{y}(t_k, \lambda) \quad k = 1, \dots, N$$

The identification method is run using Simulink/Design Optimization Toolbox on the *estimation data* with the objective to improve the BF result. Only the parameters  $\lambda$  of the linear dynamic model (9) are adjustable. For the optimization the *gradient descent* method or *method of steepest descent* is used. The coefficients in (8) have been used as starting values for the iterative search procedure.

Running this optimization a BF of 86.13% was obtained. The optimized transfer function results in:

$$G_{c, opt.}(s) = \frac{10.618 \cdot s^2 + 11.348 \cdot s + 0.519}{14.008 \cdot s^2 + 21.642 \cdot s + 2.542} \quad (10)$$

In Fig. 10 the resulting models of the first and second identification step are compared by plotting the model outputs on top of the measured output. The BF results obtained in this second step provide good performances in terms of torque estimation. Bouc–Wen models of hysteresis or higher/more complex nonlinearities could have been adopted in the identification algorithm in order to reach a better fitting to the disadvantage of simplicity. However, since the complexity of the model determines the computing time and the model is supposed to be implemented on the embedded microcontroller, a compromise has to be found between accuracy and a high update frequency of the model output. In the following section the question is pursued if a simple linear model consisting of a network of springs and dampers can be found which produces a BF which is comparable to that of the HW-model. The parameter values of the model (10) have been used as starting values for the physical networks in Section 5.

#### 5. Linear model (gray-box) identification

As introduced in Section 2, the elastomer coupling can be used as part of drive trains for example within a robotic joint drive (cmp. Fig. 1). However, the HW-model delivered by the two-steps-identification, includes static input- and output-nonlinearities which increase the complexity of the identified model. In order to design controllers for the drive setups, a simplified linear model of the elastomer would be preferable as it requires little computational power and could therefore be used on the embedded microcontrollers. Due to the nonlinearities of the HW-model, the linear part cannot be used directly for this intent. Though, it can be used as a starting point for the construction of a lumped physical model. A gray-box model identification based on a lumped model made of linear physical components (springs and dampers) has been realized to test the capacity of a linear system to deliver results comparable with those obtained with the nonlinear structures



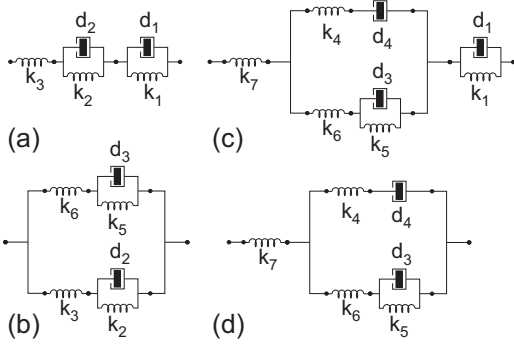


Fig. 11. Set of four lumped models for linear model identification.

Table 3

Parameter values physical network set of lumped models.

Parameter	(a) 84.76%	(b) 84.75%	(c) 84.76%	(d) 83.67%
$d_1$ (Nm s/°)	2.172	–	2.248	–
$d_2$	13.46	0.71	–	–
$d_3$	–	6.159	7.799	9.149
$d_4$	–	–	975.774	1.833
$k_1$ (Nm/°)	3.803	–	3.823	–
$k_2$	0.564	0.636	–	–
$k_3$	1.737	0.909	–	–
$k_4$	–	–	0.426	0.052
$k_5$	–	0.005	0.001	0.651
$k_6$	–	0.768	1.344	1.261
$k_7$	–	–	73.451	55.51

optimization problem becomes a problem of estimating the vector of unknown parameters  $\lambda = (d_1, \dots, k_3)$ . Starting from an initial guess, the optimization algorithm runs to find the values of the 5 parameters such that the error between the measured and the simulated response is minimized. In this process, the parameters are adjusted subject to a bound for physical consistency (spring constants and damping coefficients cannot be smaller than zero). The initial guess for the starting values of the 5 parameters  $\lambda = (d_1, \dots, k_3)$  is taken from the transfer function (10) which resulted from the second step of the black-box modeling. Eq. (10) delivers six values for the parameters  $(a_1, b_1, c_1, a_2, b_2, c_2)$ . Using the equations from (5) in combination with these six values a unique solution for  $\lambda = (d_1, \dots, k_3)$  as starting point for the parameter estimation is calculated.

### 5.1. Evaluation of resulting models

The optimization algorithm applied to the lumped parameter model shown in Fig. 11(a) produced a BF of 84.76%. Other lumped models of increasing complexity have been examined (Fig. 11(b)–(d)). For each of them the transfer function was obtained and an identification based on the *estimation data* was run with Simulink/Design Optimization Toolbox. The second model is shown in Fig. 11(b) and produced a BF of 84.75%. The third and fourth model (Fig. 11(c) and (d)) produced a BF of 84.76% and of 83.67%, respectively. The identified values of the unknown parameters for each model are reported in Table 3.

Model (c) has the same basic components as model (a) with the additional branch composed of the series connection  $k_4 - d_4$ . While model (a) has a transfer function of order 2 (see (14)), it can be shown that model (c) has a transfer function of third order. Nevertheless, the BF obtained for model (c) is the same as obtained for model (a). A reason for this is that the third order system in (c) contains a pole and a zero which cancel each other out. Therefore (c) collapses to a second order system which numerically is very close to the model in (a). This seems to confirm that a second order system is sufficient to model the dominant behavior of the elastomer coupling.

The results obtained in this section confirm that lumped parameter models composed of linear components deliver BF results comparable to the nonlinear HW-model. The comparison between models (a) and (c) shows that the first performs best while using the simpler structure.

## 6. Conclusion

Classical industrial robotics is mainly based on electric motors with large gearboxes and rigid links as it focuses on stiff systems which guarantee fast and repeatable movements with a high position accuracy, e.g. in pick-and-place applications within well defined environments.

(HW-model) (see Fig. 10). In the gray-box identification, instead of including the model structure into the optimization process, predefined networks of physical components are used and their parameters are optimized. To obtain a physical interpretation of the system, the starting point was to evaluate the transfer function (10) obtained in the former section for the linear dynamics. Based on the order of this transfer function, there are many ways to construct a matching topology consisting of linear discrete physical components. This work uses basic stress–strain models like the Maxwell model, the Kelvin–Voigt model, and the Standard Linear Solid model [24,25]. As their transfer function has the order of one, the interconnection of those models can be used to derive topologies of higher order. The simplest model that was used for the evaluation is composed of a spring and two Kelvin–Voigt models in serial (resulting in a total of 5 parameters). This model is shown in Fig. 11(a). The transfer function of the model can be obtained as series connection of these three subsystems.  $L_1(s)$  is the transfer function of the parallel setup of  $d_1$  and  $k_1$ ,  $L_2(s)$  is the transfer function of the parallel setup of  $d_2$  and  $k_2$ , while  $M(s)$  is the transfer function of the system consisting of  $k_3$ :

$$L_1(s) = \frac{1}{d_1 s + k_1} \quad (11)$$

$$L_2(s) = \frac{1}{d_2 s + k_2} \quad (12)$$

$$M(s) = \frac{1}{k_3} \quad (13)$$

The complete parametric model of the elastomer coupling in which the input is the torsion deflection angle  $\Theta_S(s)$  and the output is the torque  $T(s)$  can be written as:

$$\frac{T(s)}{\Theta_S(s)} = H(s) = \frac{1}{L_1(s) + L_2(s) + M(s)} = \frac{\bar{a}_1 s^2 + \bar{b}_1 s + \bar{c}_1}{\bar{a}_2 s^2 + \bar{b}_2 s + \bar{c}_2} \quad (14)$$

with

$$\bar{a}_1 = d_1 d_2 k_3 \quad (15a)$$

$$\bar{b}_1 = d_2 k_1 + d_1 k_2 \quad (15b)$$

$$\bar{c}_1 = k_1 k_2 k_3 \quad (15c)$$

$$\bar{a}_2 = d_1 d_2 \quad (15d)$$

$$\bar{b}_2 = d_2 k_1 + d_1 k_2 + d_1 k_3 + d_2 k_3 \quad (15e)$$

$$\bar{c}_2 = k_1 k_2 + k_1 k_3 + k_2 k_3 \quad (15f)$$

As in the former section, the identification is run using Simulink/Design Optimization Toolbox on the *estimation data*. The

The actual demand for manipulators able to share the same workspace with humans and safely interact with the environment, e.g. in fields like assistance robotics but also in industrial applications, asks for a different technical approach in design and construction. Prerequisites for this approach are lightweight construction and integrated compliance in the joints. In addition, compliance facilitates the reduction of tensions in closed kinematic chains, e.g. in walking robots or during peg-in-hole-like tasks for a robotic arm, and supports decentral control approaches [26,27]. The ability to simply guide a robot during teach-in operation and in tutoring scenarios is also simplified by a compliant system.

The traditional way to control impacts with the environment and implement compliance in a drive system is to measure the torque acting on the output using a torque sensor and use feedback control loops in order to reach the desired elasticity [4]. This, however, requires fast controllers able to cope with high torque peaks. Other approaches introduce steel springs into the drive thus supplying it with inherent elasticity and reducing the necessity to implement active stiffness control [5,10]. In order to change the inherent elasticity of the actuator online, different approaches have been developed that use additional actuators to vary the stiffness of the integrated springs [28,29]. The drawback in this approach is an increased weight of the assembly due to the support structures integrated in the mechanical setup. Additionally, elastic elements, if not adequately damped, could still present a danger due to the springback. Analog to variable stiffness actuators, also variable physical damped actuators have been developed in which the steel spring based elasticity is damped by a tunable friction contact [30]. Though extremely adaptable, the setup of these actuators is complex and therefore hard to miniaturize.

In this work, a novel rotatory drive for robotic applications which integrates inherent elasticity is presented. The design of the elastic element is based on the principle of jaw couplings in form of a sensorized elastomer coupling. The proposed coupling uses a polymer spring as source for compliance. Due to its damping characteristics this elastic element increases the safety during interactions in comparison to undamped steel spring based approaches. Furthermore, the elastomer coupling reduces the need for support structures and allows a miniaturized construction while providing a foundation to estimate load torque based on elastomer torsion. To optimize the elastomer coupling design, seven different jaw geometries were tested in FEM simulations. Results in terms of material strain and ability to produce high restoring torques at minimal fatigue were examined. One of the geometries was selected and a prototype of the coupling was manufactured and integrated into the drive.

Plasticity is an inherent property of any polymer material. Even modern elastomers with a low compression set, as the one used in this work, will introduce slack into the mechanical system after some time. To reduce this effect, the lobes of the elastomer inlay can either be bonded to their metallic counter-parts in the input- and output-hub or the lobes can be produced with oversize and squeezed into the hubs during assembly in the unbonded version. Both versions, bonded and unbonded, have been tested in this work. The bonded version is approximately 1.4 times stiffer than the unbonded.

The presence of an encoder integrated into the coupling allows to measure the angular torsion of the elastic element, thus the torques acting on the coupling can be estimated if a model of the elastic element is known. Based on this estimation, the stiffness perceived at the output link may be varied by control in dependence of the application.

Therefore, in the second part of the manuscript the identification and modeling of the coupling was performed. Starting from a data-driven black-box identification, the structure that describes the collected data best was evaluated using Matlab/System Identification

Toolbox. The Hammerstein–Wiener model (HW-model) composed of a discrete linear transfer function model with two poles and two zeros and input–output static nonlinearity represented by a second and a third order polynomial, respectively, provided the best fit.

In order to further increase the best fit, an additional optimization using a prediction-error method was adopted. Keeping the HW-model as reference structure, the parameters of the continuous time model obtained from the discrete linear transfer function were estimated using the Simulink/Design Optimization Toolbox.

A continuous time model has the advantage of a direct physical interpretation as its coefficients can be associated to parameter values of physically meaningful systems. Based on this idea, four lumped models composed of linear discrete components (springs and dampers) combined in different configurations and subject to physically consistent boundaries were tested in a gray-box identification approach. Validation results confirm that such linear models are able to describe the data delivering best-fit results comparable with the ones obtained using nonlinear structures.

In the future, the presented drive will be adopted in the construction of robotic limbs. Physiologically based control laws based on muscle models and virtual antagonistic actuation featuring antagonistic activation and co-activation could be implemented on each drive to simultaneously control position and stiffness [31,32]. Fields like prosthetics and orthotics which combine technical and biological systems may take advantage of this work and may adopt the self-contained drive.

## Acknowledgments

This work has been supported by the Federal Ministry of Education and Research (BMBF) within the BIONA program (ELAN-project to A.S.), within the Excellence Initiative of the German Research Foundation (DFG Center of Excellence “Cognitive Interaction Technology”, EXC277) and by an EU-FP7 grant (ICT-2009.2.1, No. 270182 to A.S.).

## References

- [1] M. Mason, Compliance and force control for computer controlled manipulators, *IEEE Transactions on Systems, Man and Cybernetics SMC* 11 (6) (1981) 418–432.
- [2] M. Raibert, J. Craig, Hybrid position/force control of manipulators, *Transactions of the ASME* 102 (1981) 126–133.
- [3] N. Hogan, Impedance control – an approach to manipulation. 1: theory, *Journal of Dynamic Systems Measurement and Control – Transactions of the ASME* 107 (1) (1985) 1–7.
- [4] A. Albu-Schäffer, C. Ott, G. Hirzinger, A unified passivity based control framework for position, torque and impedance control of flexible joint robots, *International Journal of Robotics Research* 26 (1) (2007) 23–39.
- [5] G. Pratt, M. Williamson, Series elastic actuators, in: *Proceedings of the IEEE/RSJ International Conference on Intelligent Robots and Systems (IROS-95)*, vol. 1, 1995, pp. 399–406.
- [6] K. Koganezawa, M. Yamazaki, Mechanical stiffness control of tendon-driven joints, in: *IEEE/RSJ International Conference on Intelligent Robots and Systems, 1999, IROS'99*, vol. 2, 1999, pp. 818–825.
- [7] N. Tsagarakis, M. Laffranchi, B. Vanderborght, D. Caldwell, A compact soft actuator unit for small scale human friendly robots, in: *IEEE International Conference on Robotics and Automation, 2009, ICRA'09*, 2009, pp. 4356–4362, <http://dx.doi.org/10.1109/ROBOT.2009.5152496>.
- [8] A. Jafari, N. Tsagarakis, B. Vanderborght, D. Caldwell, A novel actuator with adjustable stiffness (awas), in: *2010 IEEE/RSJ International Conference on Intelligent Robots and Systems (IROS)*, 2010, pp. 4201–4206, <http://dx.doi.org/10.1109/IROS.2010.5648902>.
- [9] A. Jafari, N. Tsagarakis, D. Caldwell, Awas-ii: a new actuator with adjustable stiffness based on the novel principle of adaptable pivot point and variable lever ratio, in: *2011 IEEE International Conference on Robotics and Automation (ICRA)*, 2011, pp. 4638–4643, <http://dx.doi.org/10.1109/ICRA.2011.5979994>.
- [10] O. Eiberger, S. Haddadin, M. Weis, A. Albu-Schäffer, G. Hirzinger, On joint design with intrinsic variable compliance: derivation of the dlr qa-joint., in: *2010 IEEE International Conference on Robotics and Automation (ICRA)*, 2010, pp. 1687–1694, <http://dx.doi.org/10.1109/ROBOT.2010.5509662>.
- [11] J. Paskarkeit, J. Schmitz, M. Schilling, A. Schneider, Layout and construction of a hexapod robot with increased mobility, in: *Proceedings of the 3rd IEEE*

- RAS/EMBS International Conference on Biomedical Robotics and Biomechanics, 2010, pp. 621–625.
- [12] J. Paskarkeit, J. Schmitz, M. Schilling, A. Schneider, Design of an insectoid robot as a versatile carrier for bioinspired sensors, in: Proceedings of the 13th International Conference on Climbing and Walking Robots, 2010, pp. 173–180.
  - [13] D. Vischer, O. Khatib, Design and development of high-performance torque-controlled joints, *IEEE Transactions on Robotics and Automation* 11 (4) (1995) 537–544.
  - [14] Z. Yang, A. Poo, G. Hong, A new method for implementing active stiffness control of robot manipulator by using sliding mode, in: Asia-Pacific Workshop on Advances in Motion Control Proceedings, 1993, 1993, pp. 165–170, <http://dx.doi.org/10.1109/APWAM.1993.316208>.
  - [15] A. Bicchi, G. Tonietti, Fast and soft arm tactics: dealing with the safety-performance trade-off in robot arms design and control, *IEEE Robotics and Automation Magazine* 11 (2) (2004) 22–33.
  - [16] M. Laffranchi, N. Tsagarakis, D. Caldwell, Safe human robot interaction via energy regulation control, in: IROS 2009, IEEE/RSJ International Conference on Intelligent Robots and Systems, 2009, pp. 35–41, <http://dx.doi.org/10.1109/IROS.2009.5354803>.
  - [17] S. Wolf, G. Hirzinger, A new variable stiffness design: matching requirements of the next robot generation, in: ICRA 2008, IEEE International Conference on Robotics and Automation, 2008, 2008, pp. 1741–1746, <http://dx.doi.org/10.1109/ROBOT.2008.4543452>.
  - [18] A. Albu-Schäffer, O. Eiberger, M. Grebenstein, S. Haddadin, C. Ott, T. Wimböck, S. Wolf, G. Hirzinger, Soft robotics: from torque feedback controlled light-weight robots to intrinsically compliant systems, *Robotics and Automation Magazine* 15 (3) (2008) 20–30.
  - [19] J. Sjöberg, Q. Zhang, L. Ljung, A. Benveniste, B. Deylon, P. Yves Glorennec, H. Hjalmarsson, A. Juditsky, Nonlinear black-box modeling in system identification: a unified overview, *Automatica* 31 (1995) 1691–1724.
  - [20] L. Ljung, *System Identification: Theory for the User*, 2nd ed., Prentice-Hall, Upper Saddle River, NJ, 1999.
  - [21] H. Garnier, L. Wang, *Identification of Continuous-Time Models from Sampled Data (Advances in industrial control)*, 1st ed., Springer-Verlag London Limited 2008, Incorporated, 2008, pp. 411, ISBN: 1848001614, 9781848001619.
  - [22] S. Billings, S. Fakhouri, Identification of systems containing linear dynamic and static nonlinear elements, *Automatica* 18 (1) (1982) 15–26.
  - [23] B. Haverkamp, *State space identification: Theory and practice*, Faculty of Information Technology and Systems, Delft University of Technology, The Netherlands, Delft, 2001 (Ph.D. thesis).
  - [24] R. David, *Engineering Viscoelasticity*, MIT Press, Cambridge, MA, 2001.
  - [25] M.A. Meyers, K.K. Chawla, *Mechanical Behavior of Materials*, 2nd ed., Cambridge University Press, New York, 2009, pp. 856, ISBN: 0521866758, 9780521866750.
  - [26] A. Schneider, H. Cruse, J. Schmitz, Decentralized control of elastic limbs in closed kinematic chains, *The International Journal of Robotics Research* 25 (9) (2006) 913–930.
  - [27] A. Schneider, H. Cruse, J. Schmitz, Winching up heavy loads with a compliant arm: a new local joint controller, *Biological Cybernetics* 98 (5) (2008) 413–426.
  - [28] M. Fumagalli, E. Barrett, S. Stramigioli, R. Carloni, The mvsa-ut: a miniaturized differential mechanism for a continuous rotational variable stiffness actuator, in: The Fourth IEEE RAS/EMBS International Conference on Biomedical Robotics and Biomechanics, 2012, Roma, Italy, June 24–27, 2012.
  - [29] L.C. Visser, R. Carloni, S. Stramigioli, Energy-efficient variable stiffness actuators, *IEEE Transactions on Robotics* 27 (5) (2011) 865–875.
  - [30] M. Laffranchi, N. Tsagarakis, D. Caldwell, A compact compliant actuator (compact™) with variable physical damping, in: IEEE International Conference on Robotics and Automation (ICRA), 2011, pp. 4644–4650.
  - [31] S. Annunziata, J. Paskarkeit, A. Schneider, Novel bioinspired control approaches to increase the stiffness variability in multi-muscle driven joints, *Bioinspiration and Biomimetics* 6 (4) (2013) 045003.
  - [32] S. Annunziata, A. Schneider, Physiologically based control laws featuring antagonistic muscle co-activation for stable compliant joint drives, *Applied Bionics and Biomechanics* 9 (3) (2012) 249–266, <http://dx.doi.org/10.3233/ABB-2012-0062>.

## Biographies

**Jan Paskarkeit** studied Physics with a main focus on Biophysics at Bielefeld University (Germany) where he received his Diploma in 2008. Since 2008 he has been member of the Biomechatronics group in Axel Schneider's lab where he is currently pursuing his doctoral degree. His research interests are the design of compliant, legged robots and their high-level control in outdoor scenarios.

**Salvatore Annunziata** studied Automation Engineering at the University "Federico II", Naples (Italy). He received his Master Degree in 2006. After his degree, he worked for the Engineering Control Group at the Joint European Torus (JET, Culham, England) as Visiting Scientist in 2007. He joined the Biomechatronics group in Axel Schneider's lab in 2008 where he is currently pursuing his doctoral degree. His research interests are classical and bio-inspired control of elastic joint-drives in robotics.

**Daniel Basa** studied Computer Sciences with a main focus on Natural Sciences at Bielefeld University (Germany). He received his Diploma in 2009. During his doctoral thesis, which he currently pursues in the Biomechatronics group in Axel Schneider's lab, he focuses his research interest on the acquisition of forward and inverse models for the control of elastic limbs in robotics.

**Axel Schneider** studied Electrical Engineering (University of Applied Sciences, Bielefeld, Germany) and Computer Science at Bielefeld University (Germany). At Bielefeld University, he also received his doctorate from the Faculty of Biology, where he worked in the Biological Cybernetics Lab of Holk Cruse and Josef Schmitz. Since 2007 he has been head of the Biomechatronics-group and responsible investigator in the Center of Excellence for Cognitive Interaction Technology at Bielefeld University. In April 2012 he was appointed professor for Engineering Informatics at the University of Applied Sciences, Bielefeld. His research interests are focused on bio-inspired mechatronic systems, bio-robotics and related, embedded systems.